ACS APPLIED ENERGY MATERIALS
Cite This: ACS Appl. Energy Mater. 2019, 2, 1961−1968
Article
www.acsaem.org

Microwave Synthesis of Ultrathin Nickel Hydroxide Nanosheets with Iron Incorporation for Electrocatalytic Water Oxidation

Kaili Yan,[†] Meili Sheng,[†] Xiaodong Sun,[‡,§] Chang Song,[‡,§] Zhi Cao,[‡,*,§] and Yujie Sun*[,†]

[†]Department of Chemistry, University of Cincinnati, Cincinnati, Ohio 45221, United States
[‡]State Key Laboratory of Coal Conversion, Institute of Coal Chemistry, Chinese Academy of Sciences, Taiyuan 030001, P. R. China
[§]National Energy Center for Coal to Liquids, Synfuels China Co., Ltd., Huairou District, Beijing 101400, P. R. China

Supporting Information

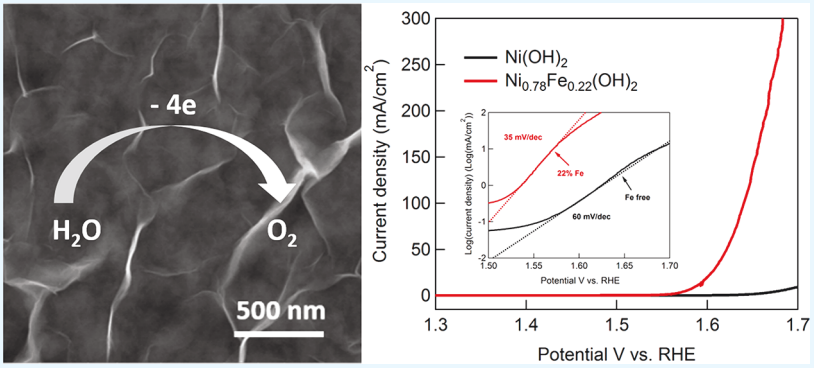

ABSTRACT: Two-dimensional ultrathin nickel hydroxide nanosheets with large surface area and excellent electronic properties have been considered as promising electrocatalysts for the oxygen evolution reaction (OER). Herein, we report a facile microwave synthetic strategy to prepare ultrathin nickel hydroxide nanosheets with thickness <1 nm. In addition, varying the iron incorporation into the parent nickel hydroxide nanosheets allows us to synthesize a series of $Ni_{1-x}Fe_x(OH)_2$ nanosheets without sacrificing the atomic thickness. Electrochemical studies demonstrate that $Fe_{0.22}Ni_{0.78}(OH)_2$ nanosheets exhibit the best OER activity, requiring an overpotential of only 315 mV to achieve 10 mA/cm^2 plus strong robustness in 1.0 M KOH. The enhanced OER performance could be mainly attributed to the intrinsically more active sites in $Fe_{0.22}Ni_{0.78}(OH)_2$. Overall, our work presents a novel and facile approach to obtain ultrathin nanosheets of nickel/iron hydroxides as competent OER electrocatalysts. The microwave synthetic approach could be readily extended to prepare many other ultrathin oxides/hydroxides for various applications.

KEYWORDS: *2D materials, ultrathin nanosheets, water oxidation, nickel hydroxides, electrocatalysis*

INTRODUCTION

Two-dimensional (2D) ultrathin nanosheets with atomic-layer thickness have attracted increasing attention due to their intriguing physical and chemical properties, such as direct band gap transition, superior electron mobility, large specific surface area, and unique surface electronic structure. Therefore, 2D ultrathin nanosheets have found applications in a variety of fields, ranging from optoelectronics, spintronics, chemical/biological sensing, supercapacitor, solar cell, lithium ion battery, to catalysis.[1−9] However, it still remains as a great challenge to synthesize ultrathin 2D nanosheets in a facile manner at a large scale. Owing to the intrinsic advantages of rapid volumetric heating, fast reaction rate, and hence reduced reaction time relative to conventional heating methods, microwave-assisted solvothermal synthesis has been recognized as a promising approach in preparing 2D ultrathin nanosheets.[10,11] Nevertheless, very rare examples have been reported utilizing microwave irradiation to synthesize ultrathin transition metal oxides/hydroxides nanosheets. Herein, we report the microwave synthesis of 2D nickel hydroxides nanosheets with atomic thickness in a very facile manner. In addition, by changing the precursor concentrations of common nickel and iron salts, we were able to synthesize a series of nickel hydroxide nanosheets with varying iron incorporation. Our work not only demonstrates the feasibility and convenience of synthesizing bimetallic hydroxides utilizing microwave irradiation but also creates a competent group of electrocatalysts for the oxygen evolution reaction (OER).

Along the ever-increasing global energy demand and diminishing fossil fuel reserves, together with negative environmental impact of fossil fuel utilization, there is a paradigm shift in energy research: exploring the capture, conversion, and utilization of carbon-free renewable energy sources is of pivotal importance to mankind's sustainable development.[12−17] Within

Received: November 28, 2018
Accepted: February 13, 2019
Published: February 13, 2019

DOI: 10.1021/acsaem.8b02067
ACS Appl. Energy Mater. 2019, 2, 1961−1968

this context, electrocatalytic water splitting to produce hydrogen and oxygen with renewable energy sources (e.g., solar and wind) has been considered as a promising approach in storing green energy in chemical forms (i.e., H_2).[18−22] However, electrocatalytic water splitting is greatly impeded by the sluggish OER, which is a four-proton/four-electron transfer process coupled with O−O bond formation. Even though expensive metal oxides like IrO_2 and RuO_2 have been reported with decent OER activity, their limited earth abundance and high cost prohibit their practical application on a large scale.[23] Hence, much effort has been devoted to exploring competent OER electrocatalysts solely composed of earth-abundant elements, such as first-row transition-metal-based oxides/hydroxides. Indeed, a large number of catalytic systems consisting of iron, cobalt, and nickel have been reported to exhibit OER performance under neutral to alkaline conditions.[24−26] For instance, Corrigan et al. found that iron impurities in alkaline electrolytes dramatically affected the OER activity of NiO_xH_y electrodes, greatly lowering the OER overpotential.[27−29] Thereafter, the beneficial role of iron incorporation into transition metal oxides/hydroxides for water oxidation has attracted intense investigations.[30−33] Recently, the groups of Boettcher,[34−38] Strasser,[39] and others have reported extensive electrochemical, spectroscopic, and computational results focusing on elucidating the impact of iron incorporation in boosting the OER performance of nickel (and cobalt) oxides/hydroxides.[40,41] The collective results showed that iron was an essential component of the active sites for OER while those hydroxides/oxyhydroxides could serve as the electronic conductive and chemically stable host to facilitate the function of these iron-related active sites.[42] It was also noticed that the underlying support would play an important role in impacting the overall OER performance; for instance, gold was found to enhance the catalytic activity of supported metal oxides/hydroxides. Therefore, it is of critical importance to avoid (or minimize) the catalyst−support synergistic effect when assessing the OER activity of an electrocatalyst.

Encouraged by the aforementioned studies, we reasoned that nickel hydroxide nanosheets with varying iron incorporation would result in superior OER performance. Although the ultrathin metal hydroxides nanosheets could be obtained by exfoliation process,[43] this method is usually uncontrollable in the uniformity of thickness and size. Recently, an oriented-attachment strategy has been reported to offer a facile production of ultrathin metal hydroxides nanomaterials.[44] However, the synthetic process is still sophisticated and time-consuming. There exist great challenges to explore a universal method to synthesizing ultrathin metal hydroxides nanomaterials in a greener manner. In this regard, microwave-assisted synthesis could provide a convenient approach to achieve free-standing 2D ultrathin nanosheets which can be coated on various inert electrodes (e.g., glassy carbon, fluorine-doped tin oxide, etc.) for electrochemical studies, avoiding a potential support−catalyst synergistic effect. In addition, it is also very convenient to control the loading amount of support-free catalysts, which provides us a great opportunity to compare catalytic activity of different electrocatalysts. Herein, we successfully synthesized ultrathin Fe-incorporated $Ni(OH)_2$ nanosheets via a microwave-assisted solvothermal method. Detailed characterization studies proved the uniform distribution of iron in the nanosheets and also confirmed the thickness was <1 nm. The OER activity of $Ni(OH)_2$ nanosheets with different percentages of iron incorporation was investigated by linear sweep voltammetry, cyclic voltammetry, electrochemical impendence spectroscopy, and long-term bulk electrolysis. It was found that $Ni_{0.78}Fe_{0.22}(OH)_2$ exhibited the highest OER activity and excellent durability among all the synthesized $Ni_{1-x}Fe_x(OH)_2$ (x = 0, 0.01, 0.05, 0.10, 0.14, 0.22, 0.29) nanosheets under alkaline conditions.

EXPERIMENTAL SECTION

Materials. Iron acetate ($Fe(C_2H_3O_2)_2$), nickel acetate ($Ni(CH_3CO_2)_2{\cdot}2H_2O$), hexamethylenetetramine (HMTA), potassium hydroxide (KOH), and Nafion 117 solution (5% in a mixture of lower aliphatic alcohols and water) were all purchased from commercial vendors and used directly without any further purification. Water was deionized (18 MΩ cm) using a Barnstead E-Pure system.

Synthesis. $2x$ (x = 0.01, 0.05, 0.10, 0.15, 0.20, and 0.30) mmol of $Fe(C_2H_3O_2)_2$, $2(1-x)$ mmol of $Ni(CH_3CO_2)_2{\cdot}2H_2O$, and 2 mmol of HMTA were added into 17 mL of deionized water under vigorous stirring to form transparent solutions. Subsequently, the solutions were heated at 120 °C for 10 min in a microwave reactor (CEM Discover Laboratory Microwave Digestion Reactor Synthesis System). Afterward, the resulting solutions were allowed to cool to room temperature, and the final products were collected by centrifuging at 6500 rpm. The obtained solids were washed with water and ethanol repeatedly and dried at room temperature under vacuum for further use.

Characterizations. SEM was conducted on a FEI QUANTA FEG 650. TEM images were collected on FEI/Philips CM-20 at an acceleration voltage of 200 kV. Elemental analysis of nickel and iron was obtained on a Thermo Electron iCAP ICP-MS. AFM measurements were performed in contact mode using a Bioscope scan head and motorized Digital Instruments (Bruker) backplane custom fitted to an inverted optical microscope. Nitrogen sorption isotherms were measured at 77 K with an autosorb iQ automated gas sorption analyzer (Quantachrome Instruments, USA). Before measurements, the samples were degassed in vacuum at 200 °C for at least 5 h. The Brunauer−Emmett−Teller (BET) method was utilized to calculate the specific surface area. XRD was recorded on a Rigaku MiniflexII desktop X-ray diffractometer. The XPS analyses were performed using a Kratos Axis Ultra instrument (Chestnut Ridge, NY) at the Surface Analysis Laboratory, Utah Nanofab. The samples were affixed on a stainless steel Kratos sample bar, loaded into the instrument's load lock chamber, and evacuated to 5×10^{-8} Torr before it was transferred into the sample analysis chamber under ultrahigh-vacuum conditions (~10^{-10} Torr). X-ray photoelectron spectra were collected using the monochromatic Al Kα source (1486.7 eV) at a 300×700 μm^2 spot size. Low-resolution survey and high-resolution region scans at the binding energy of interest were collected for each sample. To minimize charging, all samples were flooded with low-energy electrons and ions from the instrument's built-in charge neutralizer. The samples were also sputter cleaned inside the analysis chamber with 1 keV Ar^+ ions for 30 s to remove adventitious contaminants and surface oxides. XPS data were analyzed using the CASA XPS software, and energy corrections on high-resolution scans were calibrated by referencing the C 1s peak of adventitious carbon to 284.5 eV.

Electrochemical Measurements. Electrochemical measurements were performed on a computer-controlled electrochemical workstation (Gamry Interface 1000). Rotating disk electrode, Pt wire, and Ag/AgCl (saturated KCl) electrode were used as the working, counter, and reference electrode, respectively. The potential herein was referenced to the reversible hydrogen electrode (RHE) through calibration via Pt as the working electrode. Both 6 mg of catalyst and 100 μL of 5% Nafion solution were dispersed in 3 mL of a water−ethanol solution (v/v: 1/2). The above catalyst mixture was sonicated in ice-cold water for 1 h to form a homogeneous ink. Subsequently, a certain volume of the catalyst ink was drop-casted onto a rotating disk electrode (3 mm diameter, 0.07065 cm^2 geometric area). Finally, the catalyst-loaded working electrode was dried at room temperature. The KOH electrolyte was purified according to published method to remove iron impurities.[42] Chronopotentiometry measurements were performed in 1.0 M KOH at a constant current density of 10 mA/cm^2 by loading the catalyst ink onto nickel foam (0.25 cm^2) with a catalyst loading of 0.5 mg/cm^2. The

DOI: 10.1021/acsaem.8b02067
ACS Appl. Energy Mater. 2019, 2, 1961−1968

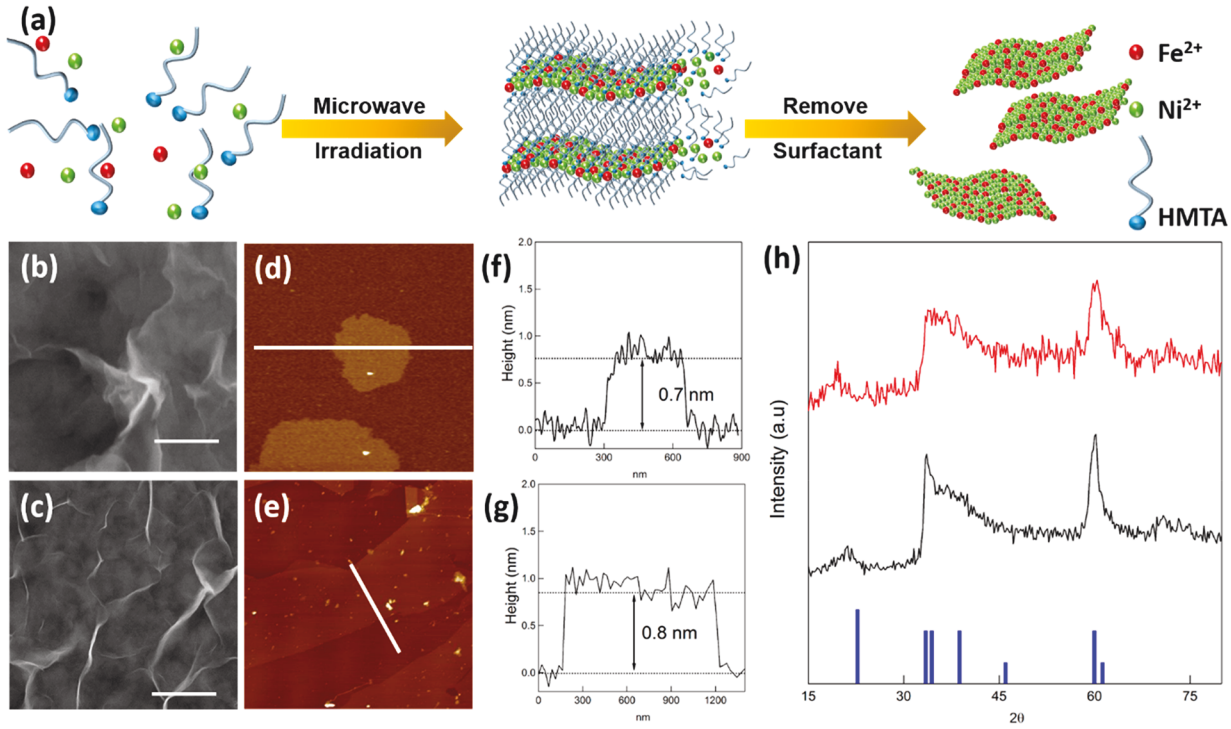

Figure 1. (a) Schematic route for the synthesis of $Ni_{1-x}Fe_x(OH)_2$ nanosheets. SEM (b, c), AFM (d, e), and the corresponding AFM height profiles (f, g) of $Ni(OH)_2$ (b, d, f) and $Ni_{0.78}Fe_{0.22}(OH)_2$ (c, e, g) nanosheets (scale bar in panels b and c: 500 nm). (h) XRD patterns of $Ni(OH)_2$ (black) and $Ni_{0.78}Fe_{0.22}(OH)_2$ (red) together with the standard XRD pattern of $Ni(OH)_2$ (blue, JCPDS card #38-0715).

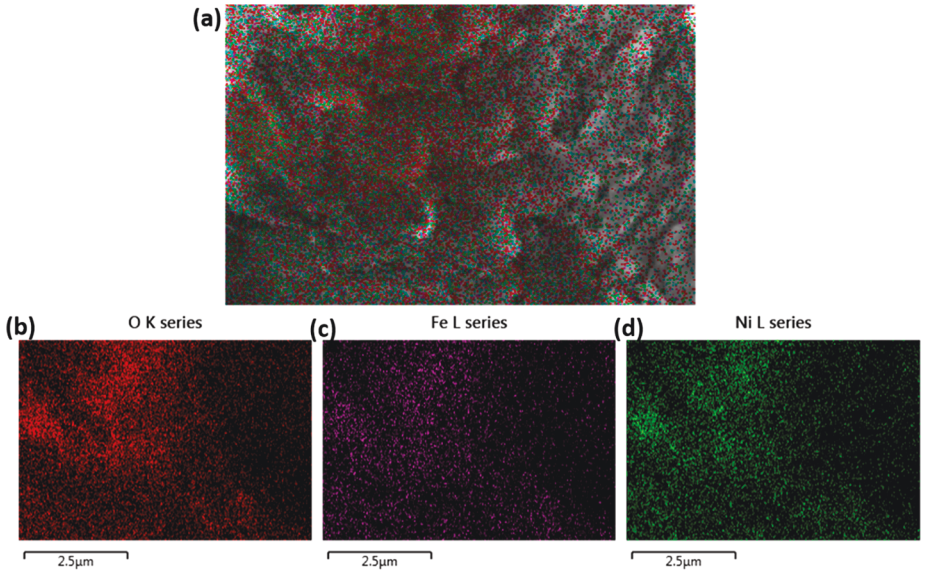

Figure 2. Elemental distribution throughout the nanosheets examined using HAADF-STEM (a) and the corresponding elemental mappings of (b) O, (c) Fe, and (d) Ni for the synthesized $Ni_{0.78}Fe_{0.22}(OH)_2$ nanosheets.

EIS measurements were performed over a frequency range from 0.1 Hz to 1 MHz at the potential range of 1.533 to 1.573 V vs RHE. The obtained EIS data were fitted with the Gamry Analyst program.

RESULTS AND DISCUSSION

The synthetic route of ultrathin Fe-incorporated $Ni(OH)_2$ nanosheets is schematically depicted in Figure 1a. In contrast to conventional solvothermal methods,[45] our microwave-assisted synthesis only required 10 min microwave irradiation (see the Experimental Section for details). Inductively coupled plasmon atomic emission spectroscopy analysis of the resulting $Ni_{1-x}Fe_x(OH)_2$ nanosheets demonstrated that the Ni/Fe ratio in the final samples was very similar to the starting molar ratio of nickel and iron acetates (Table S1) when the iron percentage was not larger than 30%. The morphology and thickness of these synthesized $Ni_{1-x}Fe_x(OH)_2$ (x = 0, 0.01, 0.05, 0.11, 0.14, 0.22, and 0.29) nanosheets were further characterized by scanning electron microscopy and atomic force microscopy. As shown in Figure 1 and Figure S1, SEM images of these synthesized samples all present the nanosheet morphology. All samples exhibit lateral dimension in the range of 500 nm to 10 μm. AFM images and the corresponding height profiles shown in Figure

DOI: 10.1021/acsaem.8b02067
ACS Appl. Energy Mater. 2019, 2, 1961−1968

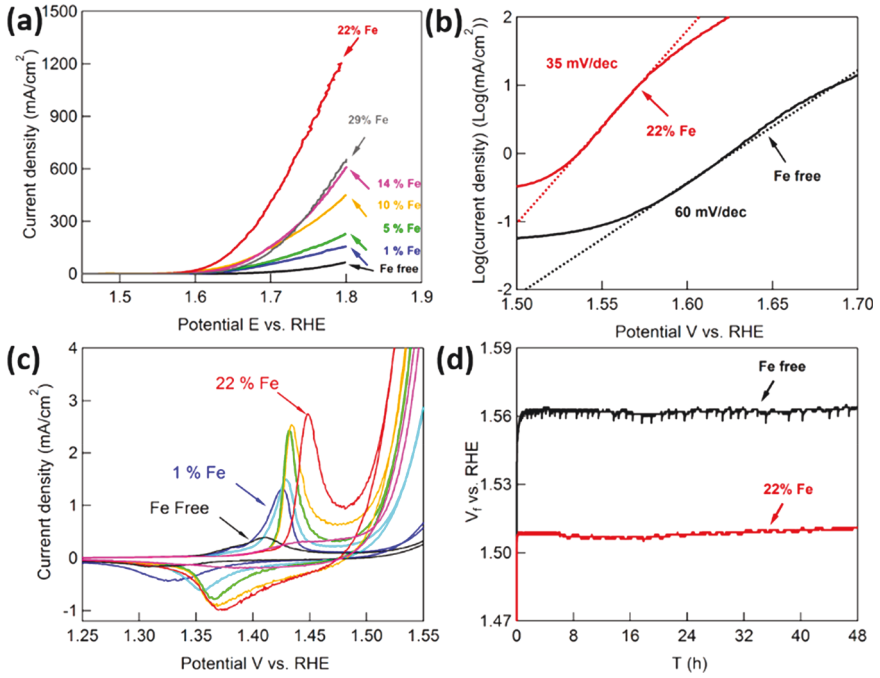

Figure 3. (a) Linear sweep voltammograms of $Ni_{1-x}Fe_x(OH)_2$ nanosheets loaded on a rotating disk electrode (RDE) in 1.0 M KOH (rotation rate = 2000 rpm and scan rate = 5 mV/s). (b) The corresponding Tafel plots of $Ni(OH)_2$ (black) and $Ni_{0.78}Fe_{0.22}(OH)_2$ (red). The dashed lines are the linear fittings. (c) Cyclic voltammograms of $Ni_{1-x}Fe_x(OH)_2$ (x = 0, 0.01, 0.05, 0.10, 0.14, 0.22, and 0.29) nanosheets loaded on a glassy carbon electrode in 1.0 M KOH (scan rate = 10 mV/s). (d) Chronopotentiometry curves of $Ni(OH)_2$ (black) and $Ni_{0.78}Fe_{0.22}(OH)_2$ (red) nanosheets loaded on nickel foams a current density of 10 mA/cm^2 in 1.0 M KOH.

1d−g measured the thickness of $Ni(OH)_2$ and $Ni_{0.78}Fe_{0.22}(OH)_2$, as approximately 0.7 and 0.8 nm, respectively. Other Fe-incorporated nickel hydroxide nanosheets possessed similar thickness (<1 nm). These results indicate that our microwave-synthesized samples were the thinnest nickel/iron hydroxides reported to date. With iron incorporation, the corresponding specific surface area measured from the Brunauer−Emmett−Teller (BET) method of N_2 adsorption−desorption isotherms (Figure S2) increased from 73 to 157 m^2/g for $Ni(OH)_2$ and $Ni_{0.78}Fe_{0.22}(OH)_2$, respectively. The elemental composition of $Ni_{0.78}Fe_{0.22}(OH)_2$ was analyzed via energy-dispersive X-ray spectrum shown in Figure S3, which only presented all the anticipated elements of Ni, Fe, O, and adventitious C. The crystallinity of $Ni(OH)_2$ and $Ni_{0.78}Fe_{0.22}(OH)_2$ nanosheets was characterized by powder X-ray diffraction measurements (Figure 1h). Both $Ni(OH)_2$ and $Ni_{0.78}Fe_{0.22}(OH)_2$ nanosheets exhibited broad peaks at 34° and 59.8°, which could be attributed to the (101) and (110) planes in $Ni(OH)_2{\cdot}0.75H_2O$ (JCPDS card #38-0715). The absence of other peaks is due to the their 2D ultrathin structures, which is a common observation for many nanosheets of atomic thickness.[46] The ultrathin nanosheets were further confirmed by using transition electron microscope (TEM). Figure S4a,c reveals the nearly transparent characteristic of the ultrathin nanosheets. High-resolution TEM (Figure S4b,d) suggests that the nanosheets were poorly crystallized, which was consistent with the observation of the selected area electron diffraction (SAED) patterns (inset in Figure S4b,d). The above results clearly confirm that the desired ultrathin nanosheets were successfully synthesized.

The elemental mapping images (Figure 2) further confirmed the uniform distribution of Ni, Fe, and O throughout the ultrathin $Ni_{0.78}Fe_{0.22}(OH)_2$ nanosheets. In addition, the composition and valence state of each element in $Ni(OH)_2$ and $Ni_{0.78}Fe_{0.22}(OH)_2$ were further probed with X-ray photoelectron spectroscopy (XPS). The XPS survey spectra of these two types of nanosheets are included in Figures S5a and S6a. All the observed peaks could be assigned to anticipated elements, such as Ni, Fe, O, and adventitious C. The high-resolution Ni 2p spectra of both samples show peaks at 871.2 and 854.5 eV, which can be assigned to the Ni $2p_{3/2}$ and $2p_{1/2}$ feature, respectively, indicating the dominant presence of Ni^{2+} in both nanosheets.[47,48] The similarity of nickel valence state in both $Ni(OH)_2$ and $Ni_{0.78}Fe_{0.22}(OH)_2$ also implied that the incorporation of iron did not alter the valence state of nickel in the parent nanosheets. In contrast to $Ni(OH)_2$, $Ni_{0.78}Fe_{0.22}(OH)_2$ exhibited well-resolved Fe 2p peaks at 709.6 and 723.4 eV, which could be assigned to the Fe^{2+} $2p_{3/2}$ and $2p_{1/2}$ feature, respectively.[49] The O 1s XPS peaks present at 528.9 and 529.5 eV for both $Ni(OH)_2$ and $Ni_{0.78}Fe_{0.22}(OH)_2$ could be associated with hydroxides and surface absorbed water.[50] Besides, to reveal the influence of Fe for Ni and O in $Ni(OH)_2$ and $Ni_{0.78}Fe_{0.22}(OH)_2$, we calculated the peak ratio of Ni and O in $Ni(OH)_2$ and $Ni_{0.78}Fe_{0.22}(OH)_2$, respectively. As shown in Table S2, after the addition of Fe in $Ni(OH)_2$, the peak ratio of Ni/O was decreased.

The electrocatalytic OER performance of the synthesized $Ni_{1-x}Fe_x(OH)_2$ (x = 0, 0.01, 0.05, 0.10, 0.14, 0.22, and 0.29) nanosheets was first evaluated via linear sweep voltammetry (LSV) in an alkaline electrolyte (1.0 M KOH). A typical three-electrode configuration was utilized, where the working electrode was prepared by loading each catalyst ink onto the surface of a rotating disk glassy carbon electrode with a loading amount of 0.07 mg/cm^2. Figure 3a compares the LSV curves of $Ni_{1-x}Fe_x(OH)_2$ at a scan rate of 5 mV/s and a rotation rate of 2000 rpm. All the $Ni_{1-x}Fe_x(OH)_2$ nanosheets were able to catalyze OER beyond 1.5 V vs RHE (reversible hydrogen electrode); however, there was a marked difference in their

DOI: 10.1021/acsaem.8b02067
ACS Appl. Energy Mater. 2019, 2, 1961−1968

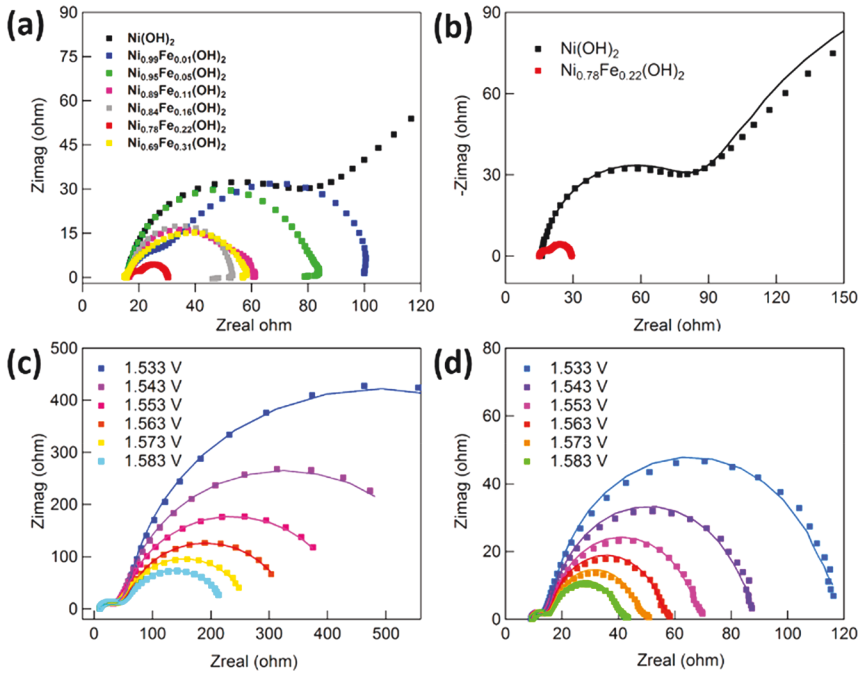

Figure 4. (a) Nyquist plots of $Ni_{1-x}Fe_x(OH)_2$ (x = 0, 0.01, 0.05, 0.10, 0.14, 0.22, and 0.29) and (b) $Ni(OH)_2$ (black) and $Ni_{0.78}Fe_{0.22}(OH)_2$ (red) at 1.543 V vs RHE in 1.0 M KOH. Electrochemical impedance spectra over a series of potentials (1.533−1.583 V vs RHE) for $Ni(OH)_2$ (c) and $Ni_{0.78}Fe_{0.22}(OH)_2$ (d) recorded in 1.0 M KOH. The solid lines are the fitting curves according to the equivalent electric circuit shown in the Supporting Information.

intrinsic OER activity. Along the increase of iron percentage, the observed current density at 1.8 V vs RHE of these $Ni_{1-x}Fe_x(OH)_2$ nanosheets increased from 67 to 1270 mA/cm^2 until x = 0.22 (Figure S7a). Further increasing the iron content resulted in a decrease in OER activity. Figure S7b further compared their activities by plotting the overpotential requirement to achieve the benchmark current density of 10 mA/cm^2. Again, a smaller overpotential was needed to produce 10 mA/cm^2 when more iron was incorporated. The smallest overpotential (315 mV) was achieved by $Ni_{0.78}Fe_{0.22}(OH)_2$, followed by an increase in overpotential requirement if more iron was included. Hence, among the seven samples of $Ni_{1-x}Fe_x(OH)_2$ (x = 0, 0.01, 0.05, 0.10, 0.14, 0.22, and 0.29), $Ni_{0.78}Fe_{0.22}(OH)_2$ demonstrated the best activity for OER. Plotting the logarithm of current density over potential for $Ni_{0.78}Fe_{0.22}(OH)_2$ and $Ni(OH)_2$ rendered a Tafel slope of 35 mV/dec for the former, which was nearly half of the Tafel slope of $Ni(OH)_2$ (60 mV/dec) as shown in Figure 3b. Such a small Tafel slope of $Ni_{0.78}Fe_{0.22}(OH)_2$ further supports its fast OER kinetics.

The large catalytic current density of the LSV curves collected on rotating disk electrode masked the redox feature of each catalyst prior to catalytic onset. To probe the possible redox peak shift of $Ni_{1-x}Fe_x(OH)_2$ with iron incorporation, we also measured the cyclic voltammograms by loading those nanosheets on a steady-state glassy carbon electrode (catalyst mass loading: 0.07 mg/cm^2). As shown in Figure 3c, the parent $Ni(OH)_2$ nanosheets showed a redox feature with an anodic peak around 1.41 V vs RHE, which could be attributed to the oxidation of Ni^{2+} to Ni^{3+} in oxyhydroxides. With only 1% iron incorporated, the anodic peak shifted to a more positive potential, 1.42 V vs RHE, accompanied by an increase in the integrated area underneath the anodic peak. The largest anodic shift and redox peak area were obtained from $Ni_{0.78}Fe_{0.22}(OH)_2$ (Figure S8). It was reported that the presence of iron would suppress the oxidation of Ni^{2+} to Ni^{3+} while simultaneously boost the intrinsic OER activity,[51] which was also evidenced from our results. Even though the specific OER active site(s) is still under debate for nickel/iron oxyhydroxides, we tentatively assumed that the size of redox wave was proportional to the number of metal sites participating in the OER electrocatalysis. Herein, we intended to estimate the turnover frequency (TOF) of our ultrathin nanosheets derived from passed charge of those redox features prior to OER catalytic current. The largest amount of integrated charge was achieved by $Ni_{0.78}Fe_{0.22}(OH)_2$ (364 mC), and a TOF of 0.33 s^{-1} was calculated at an overpotential of 0.35 V. Such a high TOF is nearly 8 times that of $Ni(OH)_2$ (Table S3).

In addition to efficiency, stability is another crucial factor when assessing the overall performance of an electrocatalyst. Long-term chronoamperometry experiments (48 h) at 10 mA/cm^2 were conducted for both $Ni(OH)_2$ and $Ni_{0.78}Fe_{0.22}(OH)_2$ samples loaded on nickel foam with a loading amount of 0.5 mg/cm^2. As plotted in Figure 3d, both $Ni(OH)_2$ and $Ni_{0.78}Fe_{0.22}(OH)_2$ nanosheets exhibited stable potential curves over the entire electrolysis period, albeit the former required an applied potential 50 mV larger than the latter. Moreover, the chronoamperometric curves of $Ni_{0.78}Fe_{0.22}(OH)_2$ and $Ni(OH)_2$ at 1.54 V (vs RHE) were collected to evaluate the durability of these electrocatalysts. As shown in Figure S9, $Ni_{0.78}Fe_{0.22}(OH)_2$ could retain a very stable current density of ∼30 mA/cm^2 over 15 h, substantially higher than that achieved on $Ni(OH)_2$ (∼10 mA/cm^2). These data not only corroborated the robustness of our ultrathin nanosheets for extended OER electrolysis but also confirmed that $Ni_{0.78}Fe_{0.22}(OH)_2$ was more active than $Ni(OH)_2$.

Because the aforementioned LSV-derived Tafel slope might overlook the impact of electric conductivity of ultrathin nanosheets in OER, we sought to further probe the intrinsic OER kinetics of these catalysts via electrochemical impedance

DOI: 10.1021/acsaem.8b02067
ACS Appl. Energy Mater. 2019, 2, 1961−1968

spectroscopy (EIS). Figure 4a complied the Nyquist plots of $Ni_{1-x}Fe_x(OH)_2$ (x = 0, 0.01, 0.05, 0.10, 0.14, 0.22, and 0.29) nanosheets collected at 1.543 V vs RHE (η = 313 mV) in 1.0 M KOH. The diameters of semicircles decreased dramatically when iron was incorporated into the parent $Ni(OH)_2$ nanosheets, arriving at the minimum diameter when the iron content was 22%. Further increasing iron percentage resulted in a higher resistance. The comparison of the Nyquist plots displayed in Figure 4b clearly showed the marked difference in resistance between $Ni(OH)_2$ and $Ni_{0.78}Fe_{0.22}(OH)_2$.

To gain a better understanding of the kinetic properties of the $Ni(OH)_2$ and $Ni_{0.78}Fe_{0.22}(OH)_2$ nanosheets, we also recorded their EIS spectra over a range of potentials associated with active O_2 evolution. The Nyquist plots of $Ni_{0.78}Fe_{0.22}(OH)_2$ and $Ni(OH)_2$ nanosheets were collected every 10 mV between 1.533 and 1.583 V vs RHE in 1.0 M KOH (Figure 4c,d). The raw impedance data could be fitted according to an equivalent circuit model depicted in Figure S10, and the simulated results were plotted as solid lines in Figures 4c and 4d for $Ni(OH)_2$ and $Ni_{0.78}Fe_{0.22}(OH)_2$, respectively. The best-fit values of the equivalent circuit elements are listed in Tables S4 and S5. By plotting $\log(R_{film})$ against applied potential, we could obtain the resistance-derived Tafel slopes (Figure S11). Indeed, a much smaller Tafel slope (43 mV/dec) of $Ni_{0.78}Fe_{0.22}(OH)_2$ relative to that (66 mV/dec) of $Ni(OH)_2$ was confirmed, further supporting the higher OER activity of the former. These Tafel slopes are similar to those reported nickel (~60 mV/dec) and nickel/iron-based OER catalysts (~40 mV/dec).[52] This excellent OER activity of $Ni_{0.78}Fe_{0.22}(OH)_2$ nanosheets could favorably compare with many reported OER catalysts consisting of nickel, iron, and cobalt (see a detailed comparison in Table S6).[53−56]

CONCLUSIONS

In summary, we have successfully synthesized a series of 2D ultrathin $Ni_{1-x}Fe_x(OH)_2$ (x = 0, 0.01, 0.05, 0.10, 0.14, 0.22, and 0.29) nanosheets via a microwave-assisted solvothermal method for the first time. Compared with traditional heating methods requiring an autoclave, our microwave-assisted synthesis was very time and energy efficient. When the iron percentage was lower than 30% in $Ni_{1-x}Fe_x(OH)_2$, the ultrathin thickness of all the resulting nanosheet samples was well maintained. A detailed electrochemical study of these ultrathin samples was conducted for water oxidation under alkaline condition. The similar morphology and thickness of these nanosheets allowed us to map out the OER activity trend as a function of iron incorporation. It was found that iron played a crucial role in enhancing the OER performance of nickel hydroxide nanosheets, with $Ni_{0.78}Fe_{0.22}(OH)_2$ exhibiting the best efficiency and strong robustness. We envision such a facile microwave-assisted synthetic approach will be applicable in preparing a variety of 2D ultrathin transition metal oxides/hydroxides for diverse applications, such as electrocatalytic O_2 reduction, CO_2 reduction, and supercapacitance.

ASSOCIATED CONTENT

Supporting Information

The Supporting Information is available free of charge on the ACS Publications website at DOI: 10.1021/acsaem.8b02067.

SEM images of $Ni_{1-x}Fe_x(OH)_2$ (x = 0.01, 0.05, 0.11, 0.14, and 0.29); nitrogen adsorption−desorption isotherms of $Ni(OH)_2$ and $Ni_{0.78}Fe_{0.22}(OH)_2$; energy-dispersive X-ray spectrum of $Ni_{0.78}Fe_{0.22}(OH)_2$; TEM images of $Ni(OH)_2$ and $Ni_{0.78}Fe_{0.22}(OH)_2$; XPS spectra of $Ni(OH)_2$: XPS spectra of $Ni_{0.78}Fe_{0.22}(OH)_2$; the electrocatalytic performance of $Ni_{1-x}Fe_x(OH)_2$ (x = 0, 0.01, 0.05, 0.11, 0.14, 0.22, and 0.29) loaded on RDE (2000 rpm) in 1.0 M purified KOH; cyclic voltammetry of $Ni_{0.78}Fe_{0.22}(OH)_2$ in 1.0 M KOH; chronoamperometric curve of $Ni_{0.78}Fe_{0.22}$ $(OH)_2$ and $Ni(OH)_2$ at 1.54 V (vs RHE); an electrical equivalent circuit used to model the OER for both $Ni(OH)_2$ and $Ni_{0.78}Fe_{0.22}(OH)_2$; Tables S1−S6 (PDF)

AUTHOR INFORMATION

Corresponding Authors

*(Y.S.) E-mail: yujie.sun@uc.edu.

*(Z.C.) E-mail: caozhi@sxicc.ac.cn.

ORCID

Yujie Sun: 0000-0002-4122-6255

Author Contributions

K.Y. and M.S. contributed equally.

Notes

The authors declare no competing financial interest.

ACKNOWLEDGMENTS

This work was supported by the National Science Foundation (CHE-1914546) and University of Cincinnati. Z.C. is grateful to the financial support from Synfuels China, Co. Ltd. Z.C. also acknowledges the innovation foundation of Institute of Coal Chemistry, Chinese Academy of Sciences, Hundred-Talent Program of Chinese Academy of Sciences, and Shanxi Hundred-Talent Program.

REFERENCES

(1) Kibsgaard, J.; Chen, Z.; Reinecke, B.-N.; Jaramillo, T. F. Engineering the surface structure of MoS_2 to preferentially expose active edge sites for electrocatalysis. *Nat. Mater.* **2012**, *11*, 963−969.

(2) Radisavljevic, B.; Whitwick, M. B.; Kis, A. Integrated circuits and logic operations based on single-layer MoS_2. *ACS Nano* **2011**, *5*, 9934−9938.

(3) Ding, S. J.; Zhang, D. Y.; Chen, J. S.; Lou, X. W. Facile synthesis of Hierarchical MoS_2 microspheres composed of few-layered nanosheets and their lithium storage properties. *Nanoscale* **2012**, *4*, 95−98.

(4) Zhang, X. D.; Zhang, J. J.; Zhao, J. Y.; Pan, B. C.; Kong, M. G.; Chen, J.; Xie, Y. Half-metallic ferromagnetism in synthetic Co_9Se_8 nanosheets with atomic thickness. *J. Am. Chem. Soc.* **2012**, *134*, 11908−11911.

(5) Mak, K. F.; Lee, C.; Hone, J.; Shan, J.; Heinz, T. F. Atomically thin MoS_2: a new direct-gap semiconductor. *Phys. Rev. Lett.* **2010**, *105*, 136805.

(6) Li, T.; Galli, G. Electronic properties of MoS_2 nanoparticles. *J. Phys. Chem. C* **2007**, *111*, 16192−16196.

(7) Benameur, M. M.; Radisavljevic, B.; Héron, J. S.; Sahoo, S.; Berger, H.; Kis, A. Visibility of dichalcogenide nanolayers. *Nanotechnology* **2011**, *22*, 125706.

(8) Zhang, Y.; Tang, T.-T.; Girit, C.; Hao, Z.; Martin, M. C.; Zettl, A.; Crommie, M. F.; Shen, Y. R.; Wang, F. Direct observation of a widely tunable bandgap in bilayer graphene. *Nature* **2009**, *459*, 820−823.

(9) Lee, H. S.; Min, S.-W.; Chang, Y.-G.; Park, M. K.; Nam, T.; Kim, H.; Kim, J. H.; Ryu, S.; Im, S. MoS_2 nanosheet phototransistors with thickness-modulated optical energy gap. *Nano Lett.* **2012**, *12*, 3695−3700.

(10) Wu, L.; Bi, J.; Li, Z.; Wang, X.; Fu, X. Rapid preparation of Bi_2WO_6 photocatalyst with nanosheet morphology via micro-wave-assisted solvothermal synthesis. *Catal. Today* **2008**, *131*, 15−20.

(11) Murugan, A.; Muraliganth, T.; Manthiram, A. Rapid, facile microwave-solvothermal synthesis of graphene nanosheets and their polyaniline nanocomposites for energy strorage. *Chem. Mater.* **2009**, *21*, 5004−5006.
(12) Dresselhaus, M. S.; Thomas, I.-L. Alternative energy technologies. *Nature* **2001**, *414*, 332−337.
(13) Turner, J. A. Sustainable hydrogen production. *Science* **2004**, *305*, 972−974.
(14) Lewis, N. S.; Nocera, D. G. Powering the planet: Chemical challenges in solar energy utilization. *Proc. Natl. Acad. Sci. U. S. A.* **2006**, *103*, 15729−15735.
(15) Song, F. Z.; Zhu, Q. L.; Tsumori, N.; Xu, Q. Diamine-alkalized reduced graphene oxide: immobilization of sub-2 nm palladium nanoparticles and optimization of catalytic activity for dehydrogenation of formic acid. *ACS Catal.* **2015**, *5*, 5141−5144.
(16) Song, F. Z.; Zhu, Q. L.; Xu, Q. Monodispersed PtNi nanoparticles deposited on diamine-alkalized graphene for highly efficient dehydrogenation of hydrous hydrazine at room temperature. *J. Mater. Chem. A* **2015**, *3*, 23090−23094.
(17) Cook, T. R.; Dogutan, D. K.; Reece, S. Y.; Surendranath, Y.; Teets, T. S.; Nocera, D. G. Solar energy supply and storage for the legacy and nonlegacy worlds. *Chem. Rev.* **2010**, *110*, 6474−6502.
(18) Jiang, N.; You, B.; Sheng, M. L.; Sun, Y. J. Electrodeposited cobalt-phosphorous-derived films as competent bifunctional catalysts for overall water splitting. *Angew. Chem.* **2015**, *127*, 6349−6352.
(19) You, B.; Jiang, N.; Sheng, M. L.; Gul, S.; Yano, J.; Sun, Y. J. High-performance overall water splitting electrocatalysts derived from cobalt-based metal-organic frameworks. *Chem. Mater.* **2015**, *27*, 7636−7642.
(20) You, B.; Jiang, N.; Sheng, M.; Bhushan, M. W.; Sun, Y. J. Hierarchically porous urchin-like Ni_2P superstructures sup-ported on nickel foam as efficient bifunctional electrocatalysts for overall water splitting. *ACS Catal.* **2016**, *6*, 714−721.
(21) Wang, J.; Cui, W.; Liu, Q.; Xing, Z.; Asiri, A. M.; Sun, X. Recent progress in cobalt-based heterogeneous catalysts for electro-chemical water splitting. *Adv. Mater.* **2016**, *28*, 215−230.
(22) Fominykh, K.; Feckl, J. M.; Sicklinger, J.; Doblinger, M.; Bocklein, S.; Ziegler, J.; Peter, L.; Rathousky, J.; Scheidt, E.-W.; Bein, T.; Fattakhova-Rohlfing, D. Ultrasmall dispersible crystalline nickel oxide nanoparticles as high-performance catalysts for electrochemical water splitting. *Adv. Funct. Mater.* **2014**, *24*, 3123−3129.
(23) Reier, T.; Oezaslan, M.; Strasser, P. Electrocatalytic oxygen evolution reaction (OER) on Ru, Ir, and Pt catalysts: a comparative study of nanoparticles and bulk materials. *ACS Catal.* **2012**, *2*, 1765−1772.
(24) Fang, Y.-H.; Liu, Z.-P. Mechanism and Tafel lines of electro-oxidation of water to oxygen on RuO_2 (110). *J. Am. Chem. Soc.* **2010**, *132*, 18214−18222.
(25) Song, F.; Hu, X. Ultrathin cobalt-manganese layered double hydroxide is an efficient oxygen evolution catalyst. *J. Am. Chem. Soc.* **2014**, *136*, 16481−16484.
(26) Osada, M.; Sasaki, T. Two-dimensional dielectric nanosheets: novel nanoelectronics from nanocrystal building blocks. *Adv. Mater.* **2012**, *24*, 210−228.
(27) Bischoff, M. Molten carbonate fuel cells: A high temperature fuel cell on the edge to commercialization. *J. Power Sources* **2006**, *160*, 842−845.
(28) Jović, V. D.; Jović, B. M.; Lačnjevac, U. Č.; Krstajić, N. V.; Zabinski, P.; Elezović, N. R. Accelerated service life test of electrodeposited NiSn alloys as bifunctional catalysts for alkaline water electrolysis under industrial operating conditions. *J. Electroanal. Chem.* **2018**, *819*, 16−25.
(29) Munshi, M.; Tseung, A.; Parker, J. The dissolution of iron from the negative material in pocket plate nickel-cadmium batteries. *J. Appl. Electrochem.* **1985**, *15*, 711−717.
(30) Shin, H.; Xiao, H.; Goddard, W.-A. In silico discovery of new dopants for Fe-doped Ni oxyhydroxide ($Ni_{1-x}Fe_xOOH$) catalysts for oxygen evolution reaction. *J. Am. Chem. Soc.* **2018**, *140*, 6745−6748.
(31) Corrigan, D. A. The catalysis of the oxygen evolution reaction by iron impurities in thin film nickel oxide electrodes. *J. Electrochem. Soc.* **1987**, *134*, 377−384.
(32) Młynarek, G.; Paszkiewicz, M.; Radniecka, A. J. The effect of ferric ions on the behaviour of a nickelous hydroxide electrode. *J. Appl. Electrochem.* **1984**, *14*, 145−149.
(33) Gong, M.; Wang, D. Y.; Chen, C. C.; Hwang, B. J.; Dai, H. A mini review on nickel-based electrocatalysts for alkaline hydrogen evolution reaction. *Nano Res.* **2016**, *9*, 28−46.
(34) Trotochaud, L.; Young, S. L.; Ranney, J. K.; Boettcher, S. W. Nickel-iron oxyhydroxide oxygen-evolution electrocatalysts: the role of intentional and incidental iron incorporation. *J. Am. Chem. Soc.* **2014**, *136*, 6744−6753.
(35) Burke, M. S.; Kast, M. G.; Trotochaud, L.; Smith, A. M.; Boettcher, S. W. Cobalt-iron (oxy)hydroxide oxygen evolution electrocatalysts: the role of structure and composition on activity, stability, and mechanism. *J. Am. Chem. Soc.* **2015**, *137*, 3638−3648.
(36) Burke, M. S.; Zou, S.; Enman, L. J.; Kellon, J. E.; Gabor, C. A.; Pledger, E.; Boettcher, S. W. Revised oxygen evolution reaction activity trends for first-row transition-metal (oxy)hydroxides in alkaline media. *J. Phys. Chem. Lett.* **2015**, *6*, 3737−3742.
(37) Zou, S.; Burke, M. S.; Kast, M. G.; Fan, J.; Danilovic, N.; Boettcher, S. W. Fe (oxy)hydroxide oxygen evolution reaction electrocatalysis: Intrinsic activity and the roles of electrical conductivity, substrate, and dissolution. *Chem. Mater.* **2015**, *27*, 8011−8020.
(38) Enman, L. J.; Burke, M. S.; Batchellor, A. S.; Boettcher, S. W. Effects of intentionally incorporated metal cations on the oxygen evolution electrocatalytic activity of nickel (oxy)hydroxide in alkaline media. *ACS Catal.* **2016**, *6*, 2416−2423.
(39) Görlin, M.; Chernev, P.; Ferreira de Araújo, J.; Reier, T.; Dresp, S.; Paul, B.; Krähnert, R.; Dau, H.; Strasser, P. Oxygen evolution reaction dynamics, faradaic charge efficiency, and the active metal redox states of Ni-Fe oxide water splitting electrocatalysts. *J. Am. Chem. Soc.* **2016**, *138*, 5603−5614.
(40) Friebel, D.; Louie, M. W.; Bajdich, M.; Sanwald, K. E.; Cai, Y.; Wise, A.-W.; Cheng, M.-J.; Sokaras, D.; Weng, T.-C.; Alonso-Mori, R.; Davis, R. C.; Bargar, J. R.; Nørskov, J. K.; Nils-son, A.; Bell, A. T. Identification of highly active Fe sites in (Ni, Fe)OOH for electrocatalytic water splitting. *J. Am. Chem. Soc.* **2015**, *137*, 1305−1313.
(41) Klaus, S.; Cai, Y.; Louie, M.-W.; Trotochaud, L.; Bell, A. T. Effects of Fe electrolyte impurities on $Ni(OH)_2$/NiOOH structure and oxygen evolution activity. *J. Phys. Chem. C* **2015**, *119*, 7243−7254.
(42) Trotochaud, L.; Young, S. L.; Ranney, J. K.; Boettcher, S. W. Nickel-iron oxyhydroxide oxygen-evolution electrocatalysts: the role of intentional and incidental iron incorporation. *J. Am. Chem. Soc.* **2014**, *136*, 6744−6753.
(43) Yin, H.; Tang, Z. Ultrathin two-dimensional layered metal hydroxides: an emerging platform for advanced catalysis, energy conversion and storage. *Chem. Soc. Rev.* **2016**, *45*, 4873−4891.
(44) Gao, S.; Sun, Y.; Lei, F.; Liang, L.; Liu, J.; Bi, W.; Pan, B.; Xie, Y. Ultrahigh Energy Density Realized by a Single-Layer β-$Co(OH)_2$ All-Solid-State Asymmetric Supercapacitor. *Angew. Chem., Int. Ed.* **2014**, *53*, 12789−12793.
(45) Ida, S.; Shiga, D.; Koinuma, M.; Matsumoto, Y. Synthesis of hexagonal nickel hydroxide nanosheets by exfoliation of layered nickel hydroxide intercalated with dodecyl sulfate ions. *J. Am. Chem. Soc.* **2008**, *130*, 14038−10439.
(46) Sun, Y.; Gao, S.; Lei, F.; Liu, J.; Liang, L.; Xie, Y. Atomically-thin non-layered cobalt oxide porous sheets for highly efficient oxygen-evolving electrocatalysts. *Chem. Sci.* **2014**, *5*, 3976−3982.
(47) Nesbitt, H.-W.; Legrand, D.; Bancroft, G.-M. Interpretation of Ni_2P XPS spectra of Ni conductors and Ni insulators. *Phys. Chem. Miner.* **2000**, *27*, 357−366.
(48) Lee, J.-W.; Ahn, T.; Soundararajan, D.; Ko, J.-M.; Kim, J.-D. Non-aqueous approach to the preparation of reduced graphene oxide/α-$Ni(OH)_2$ hybrid composites and their high capacitance behavior. *Chem. Commun.* **2011**, *47*, 6305−6307.

DOI: 10.1021/acsaem.8b02067
ACS Appl. Energy Mater. 2019, 2, 1961−1968

(49) Yang, S.; Guo, Y.; Yan, N.; Wu, D.; He, H.; Qu, Z.; Jia, J. Elemental mercury capture from flue gas by magnetic Mn-Fe spinel: effect of chemical heterogeneity. *Ind. Eng. Chem. Res.* **2011**, *50*, 9650−9656.
(50) Jiang, H.; Guo, Y.; Wang, T.; Zhu, P.-L.; Yu, S.; Yu, Y.; Fu, X.-Z.; Sun, R.; Wong, C.-P. Electrochemical fabrication of $Ni(OH)_2$/Ni 3D porous composite films as integrated capacitive electrodes. *RSC Adv.* **2015**, *5*, 12931−12936.
(51) Louie, M.-W.; Bell, A. T. An investigation of thin-film Ni-Fe oxide catalysts for the electrochemical evolution of oxygen. *J. Am. Chem. Soc.* **2013**, *135*, 12329−12337.
(52) Dionigi, F.; Strasser, P. NiFe-Based (oxy)hydroxide catalysts for oxygen evolution reaction in non-acidic electrolytes. *Adv. Energy Mater.* **2016**, *6*, 1600621.
(53) Xu, K.; Chen, P.; Li, X.; Tong, Y.; Ding, H.; Wu, X.; Chu, W.; Peng, Z.; Wu, C.; Xie, Y. Metallic nickel nitride nanosheets realizing enhanced electrochemical water oxidation. *J. Am. Chem. Soc.* **2015**, *137*, 4119−4125.
(54) Kuai, L.; Geng, J.; Chen, C.; Kan, E.; Liu, Y.; Wang, Q.; Geng, B. A reliable aerosol-spray-assisted approach to produce and optimize amorphous metal oxide catalysts for electrochemical water splitting. *Angew. Chem.* **2014**, *126*, 7677−7681.
(55) Zhang, Y.; Cui, B.; Zhao, C.; Lin, H.; Li, J. Co-Ni layered double hydroxides for water oxidation in neutral electrolyte. *Phys. Chem. Chem. Phys.* **2013**, *15*, 7363−7369.
(56) Chen, S.; Duan, J.; Ran, J.; Jaroniec, M.; Qiao, S. Z. N-doped graphene film-confined nickel nanoparticles as a highly efficient three-dimensional oxygen evolution electrocatalyst. *Energy Environ. Sci.* **2013**, *6*, 3693−3699.

DOI: 10.1021/acsaem.8b02067
ACS Appl. Energy Mater. 2019, 2, 1961−1968